

Modeling the light response of an optically readout GEM based TPC for the CYGNO experiment

Fernando Dominques Amaro¹, Rita Antonietti^{2,3},
Elisabetta Baracchini^{4,5}, Luigi Benussi⁶, Stefano Bianco⁶,
Roberto Campagnola⁶, Cesidio Capoccia⁶, Michele Caponero^{6,9},
Gianluca Cavoto^{7,8}, Igor Abritta Costa⁶, Antonio Croce⁶,
Emiliano Dané⁶, Melba D'Astolfo^{4,5}, Giorgio Dho⁶,
Flaminia Di Giambattista^{4,5}, Emanuele Di Marco⁷,
Giulia D'Imperio⁷, Joaquim Marques Ferreira dos Santos¹,
Davide Fiorina^{4,5}, Francesco Iacoangeli⁷, Zahoor Ul Islam^{4,5},
Herman Pessoa Lima Júnior^{4,5}, Ernesto Kemp¹⁰, Francesca Lewis⁸,
Giovanni Maccarrone⁶, Rui Daniel Passos Mano¹,
Robert Renz Marcelo Gregorio¹¹, David José Gaspar Marques^{4,5},
Luan Gomes Mattosinhos de Carvalho¹², Giovanni Mazzitelli⁶,
Alasdair Gregor McLean¹¹, Pietro Meloni^{2,3}, Andrea Messina^{7,8},
Cristina Maria Bernardes Monteiro¹, Rafael Antunes Nobrega¹²,
Igor Fonseca Pains¹², Matteo Pantalena⁸, Emiliano Paoletti⁶,
Luciano Passamonti⁶, Fabrizio Petrucci^{2,3}, Stefano Piacentini^{4,5},
Davide Piccolo⁶, Daniele Pierluigi⁶, Davide Pinci^{7,a}, Atul Prajapati^{4,5},
Francesco Renga⁷, Rita Cruz Roque¹, Filippo Rosatelli⁶,
Alessandro Russo⁶, Sabrina Salamino⁸, Giovanna Saviano^{6,13},
Federico Francesco Scamporlino⁸, Angelo Serrecchia⁸,
Pedro Alberto Oliveira Costa Silva¹, Neil John Curwen Spooner¹¹,
Roberto Tesauro⁶, Sandro Tomassini⁶, Samuele Torelli^{4,5},
Donatella Tozzi^{7,8}

¹LIBPhys, Department of Physics, University of Coimbra, 3004-516 Coimbra, Portugal;

²Istituto Nazionale di Fisica Nucleare, Sezione di Roma TRE, 00146, Roma, Italy;

³Dipartimento di Matematica e Fisica, Università Roma TRE, 00146, Roma, Italy;

⁴Gran Sasso Science Institute, 67100, L'Aquila, Italy;

⁵Istituto Nazionale di Fisica Nucleare, Laboratori Nazionali del Gran Sasso, 67100, Assergi, Italy;

⁶Istituto Nazionale di Fisica Nucleare, Laboratori Nazionali di Frascati, 00044, Frascati, Italy;

⁷Istituto Nazionale di Fisica Nucleare, Sezione di Roma, 00185, Rome, Italy;

⁸Dipartimento di Fisica, Sapienza Università di Roma, 00185, Roma, Italy;

⁹ENEA Centro Ricerche Frascati, 00044, Frascati, Italy;

¹⁰Universidade Estadual de Campinas - UNICAMP; Campinas 13083-859; SP; Brazil

¹¹Department of Physics and Astronomy, University of Sheffield, Sheffield, S3 7RH, UK;

¹²Universidade Federal de Juiz de Fora, Faculdade de Engenharia, 36036-900, Juiz de Fora, MG, Brasil;

¹³Dipartimento di Ingegneria Chimica, Materiali e Ambiente, Sapienza Università di Roma, 00185, Roma, Italy;

Internal v1: 2023-03-02

1 **Abstract** The use of gaseous Time Projection Cham- 8
2 bers enables the detection and the detailed study of rare 9
3 events due to particles interactions with the atoms of 10
4 the gas with energy releases as low as a few keV. Due to 11
5 this capability, these instruments are being developed 12
6 for applications in the field of astroparticle physics, such 13
7 as the study of dark matter and neutrinos. To readout 14

events occurring in the sensitive volume with a high
granularity, the CYGNO collaboration is developing a
solution where the light generated during the avalanche
processes occurring in a multiplication stage based on
Gas Electron Multiplier (GEM) is read out by optical
sensors with very high sensitivity and spatial resolution.

To achieve a high light output, gas gain values of
the order of 10^5 - 10^6 are needed. Experimentally, a de-
pendence of the detector response on the spatial density

^ae-mail: davide.pinci@roma1.infn.it

of the charge collected in the GEM holes has been observed, indicating a gain-reduction effect likely caused by space-charge buildup within the multiplication channels.

This paper presents data collected with a prototype featuring a sensitive volume of about two liters, together with a model developed by the collaboration to describe and predict the gain dependence on charge density. A comparison with experimental data shows that the model accurately reproduces the gain behaviour over nearly one order of magnitude, with a percent-level precision.

1 Introduction

The CYGNO project [1] is aiming at the realisation of a cubic meter scale gaseous Time Projection Chamber (TPC) operating at atmospheric pressure for the search and study of rare events such as neutrino interactions or weakly-interacting massive particle (WIMP) scattering [2, 3, 4]. Gaseous TPC are very suitable devices for these kinds of research: they offer the possibility of instrumenting large sensible volumes with a reduced number of readout channels compared to other approaches while retaining the possibility of having a complete reconstruction of the events within them with high spatial and energy resolutions [5].

Moreover, in a gas, a nuclear or electron recoil with an energy of a few of keV would travel for hundreds to thousands of microns, leaving a trail of ionised atoms and free electrons that can be exploited to produce a detectable signal and allow for a three dimensional reconstruction of the particle direction.

2 Optical readout

In this respect the CYGNO project has conducted an R&D program to evaluate the feasibility and the performance of a gaseous TPC, with an amplification based on a Gas Electron Multiplier (GEM, [6]) stage, with an optical readout [7, 8, 9]. The detector is based on the acquisition of the light produced by electroluminescence during the multiplication processes in the GEM channels with a readout system that combines the high spatial resolution of the Active Pixel Sensors (APS) and the time resolution of photomultipliers [10, 1]. The main advantage of this approach is related to the very excellent performance that scientific CMOS-based (sCMOS) APS are able to provide:

- a high granularity with millions of independent readout pixels;

- an average noise level and a sensitivity allowing the detection of individual photons with high efficiency;

Moreover, the optical coupling gives the possibility to keep the sensor out of the sensitive volume (no interference with HV operation and lower gas contamination) and, by means of a suitable lens system, it is possible to acquire large surfaces with small sensors (reducing the setup complexity).

The geometrical optical acceptance ϵ_{Ω} of a lens system, defined as the fraction of emitted photons reaching the sensor, depends on the lens aperture a^1 and the system magnification δ (the ratio between the captured area and the sensor area). It can be expressed as:

$$\epsilon_{\Omega} = \frac{1}{(4(\delta + 1) \cdot a)^2} \quad (1)$$

Typical setups with δ of the order of few tens and a around 1 yield values of $\epsilon_{\Omega} = 10^{-3}$ - 10^{-4} .

2.1 The He and CF₄ based gas mixture

According to previous studies [8, 11], electroluminescence spectra of CF₄ based mixtures show two main maxima: one around a wavelength of 300 nm and one around 620 nm. Since this second wavelength matches the region of largest quantum efficiency of silicon-based light sensors, CF₄-based gas mixtures are the most commonly used for the optical readout.

In particular, the CYGNO collaboration has used a CF₄ and helium gas mixture since the beginning. Helium, thanks to its light nucleus, allows for large momentum transfers in collisions with particles of GeV-scale mass, making it especially suitable for studying low-mass WIMP interactions.

The use of a proportion 60/40 between He and CF₄ makes it possible to operate under very stable conditions even with high gain in the amplification stages, leading to the production of up to 2-3 millions of secondary electrons per primary one [12].

An average energy loss needed to produce an electron pair (w value) of 35 eV is obtained by taking the weighted average of the He and the CF₄ work functions [13, 14, 15, 16].

For this particular gas mixture, 0.07 photons are expected to be produced per secondary electron in the avalanche [8, 17]. Taking into account the values of ϵ_{Ω}

¹with the *aperture* of a lens (usually also denoted as #) in optics is indicated the ratio between the focal length (FL) and the diaphragm diameter (D): $a = \text{FL}/D$

evaluated above, such a large amount of secondary electrons ensures the collection of a few photons per electronvolt released into the gas, resulting in a high detection efficiency even for tiny energy releases.

On the other hand, the large amount of charges in the multiplication region is very likely responsible of the non-linear phenomena observed in the detector's response.

3 Experimental setup

In recent years, the CYGNO collaboration has developed several prototypes for R&D studies on this technology, with sensitive volumes ranging from 0.1 liters (ORANGE, [18,19,20,10] and MANGO [21,22]), to 7 liters (LEMON [23]) and then to 50 liters (LIME [24]). A last prototype (called GIN) with a sensitive volume of approximately two liters, designed as a flexible and multi-purpose device for R&D and tests, was recently realised by the INFN Laboratori Nazionali di Frascati (LNF)

3.1 GIN detector

The main components of the GIN prototype, depicted in Fig. 1, are described in the following subsections.

3.1.1 Vessel, Field Cage and GEM stack

The gas vessel is made of a transparent poly-methyl methacrylate (PMMA) parallelepipedal box.

Within the acrylic vessel, a series of seventeen 10×10 cm² squared copper rings electrically connected in series through resistors and maintained at progressively increasing potential values act as electrodes of an electric field cage (FC). The FC is closed on one side by a 10×10 cm² copper cathode, which defines the lowest potential, and on the other side by a structure of three 10×10 cm² GEMs. These have bi-conical multiplication channels with an internal diameter of $50 \mu\text{m}$, an external one of $70 \mu\text{m}$ and pitch of $140 \mu\text{m}$. The three GEMs are placed 5 mm apart from the first field cage coil and 2 mm apart from each other. The gaps between the three GEMs are usually referred to as *transfer gaps*. This configuration generates within the field cage a uniform electric field (called *drift field* E_{Drift}), oriented orthogonally to the cathode and GEM planes, that guides the ionization electrons produced by charged particles traversing the gas towards the anodic GEMs stack. The drift field region spans 253 mm in length making the sensitive gas volume of the GIN prototype to be 2.2 liters.

Electrical potentials at the various electrodes of the detector are supplied by two generators:

- cathode: an ISEG *HPn 500*² provides up to 50 kV and 7 mA with negative polarity and ripple $< 0.2\%$;
- GEM electrodes: CAEN *A1515TG*³ board with individual floating channels supplies the voltages (up to 1 kV with 20 mV precision);

By means of these two power suppliers, the following electrostatic configuration is setup in GIN:

- a constant E_{Drift} with a typical value of 1.0 kV/cm in the sensitive volume;
- a constant *transfer field* in the transfer gaps between the GEMs ($E_{\text{Transf}} = 2.5$ kV/cm);
- the voltage difference across the two sides of each GEM (V_{GEM}) that was changed accordingly to the different test needs.

3.1.2 Light sensors

The light produced in the multiplication channels of the last GEM is transmitted out of the vessel by a $200 \mu\text{m}$ thick PET window. A black optical bellow is mounted on the external side of the window and allows for a safe transmission of the light signal to the optical sensors:

- the ORCA-Fusion⁴ scientific CMOS camera with 2304×2304 pixels of $6.5 \times 6.5 \mu\text{m}^2$ placed at a distance of 22.3 cm from the last GEM, captures an 11.52×11.52 cm² image, able to detect photons over the whole visible spectrum with quantum efficiency above 60% and a peak of 80% at 500 nm. In this configuration, the geometrical acceptance ϵ_{Ω} results to be 9.2×10^{-4} and each pixel can frame an area of $50 \times 50 \mu\text{m}^2$.
- two Hamamatsu R1894 photomultipliers, with a 10 mm diameter, with a spectral response from 300 nm to 850 nm and a QE of about 1% at 620 nm.

3.1.3 Gas supply system

The gas vessel is continuously flushed at a rate of 150 cc/min with a mixture, obtained from bottles of pure gases: He with a rate of 90 cc/min and CF₄ with a rate of 60 cc/min. No recirculation of the gas is foreseen and the output gas is sent to an exhaust line connected to

²For more details, please visit <https://iseg-hv.com/en/home>

³For more details, please visit <https://www.caen.it/families/universal-multichannel-system/>

⁴For more details please visit <https://www.hamamatsu.com/eu/en/product/cameras/cmos-cameras/C14440-20UP.html>

the external environment via a water-filled bubbler ensuring an over-pressure of approximately 3 mbar, relative to the external atmospheric pressure.

3.1.4 Source window

The upper surface of the vessel features a thin window, 2 cm wide and 23 cm long perpendicular to the GEM plane, sealed by a 125 μm thick layer of ethylene tetrafluoroethylene (ETFE). This window permits the entry of low-energy photons (down to the keV range) into the gas volume from external radioactive sources utilized for calibration purposes.

A manually controlled trolley is mounted above this window and is capable of moving back and forth on a predefined track along the z axis. It serves as a holder for the radioactive source and enables its movement, positioned 8 cm above the sensitive volume, ranging from $z=1$ cm to $z=24$ cm from the GEMs.

3.1.5 Faraday cage

The light tightness and electrical shield of the detector is ensured by an external Faraday cage made of a 3 mm thick aluminum metal box suitably equipped with feed-through connections for the high voltages required for the GEMs, cathode and PMT and for the gas piping. A rod, free to enter through the rear face, allows the movement of the source trolley.

4 Data taking

To study the behaviour of the detector light response, the signals produced by the interaction of X-rays in the gas volume were acquired and analysed.

4.1 Data acquisition system

The data acquisition is implemented by using an integrated system within the Midas framework⁵. PMT analogue signals are routed to a discriminator and then to a logic module, which generates a trigger signal based on the coincidence of the signals above threshold from the two PMTs. A dedicated data acquisition PC is connected via two USB 3.0 ports to both the camera and a VME crate containing I/O register modules for triggering and control functions. Although the DAQ system is designed to accommodate digitizers for acquiring PMT signal waveforms, this article focuses exclusively on the analysis of 2D image obtained by the camera.

⁵for more details please visit <https://daq00.triumf.ca/MidasWiki/index.php/MainPage>

4.2 Detector Operation

The measurements reported in this paper were carried out at the INFN-LNF laboratories. The detector was operated inside an experimental hall where the temperature varied in a range between 295 K and 300 K and the atmospheric pressure between 970 mbar and 1000 mbar for the entire duration of the measurements. The typical working conditions of the detector are reported in Table 1.

Table 1 Summary of the typical operating condition of the GIN detector during the data takings.

Parameter	Typical value
Drift Field	1.0 kV/cm
GEM Voltage	420 V - 440 V
Transfer Field	2.5 kV/cm
Gas Flow	9.0 l/h
PMT Threshold	15 mV

4.3 Data acquisition strategy

The camera supports adjustable exposure time. Following an optimization designed to balance the average number of events per image, keeping it low enough to minimize the probability of overlapping events, yet high enough to avoid an excessive number of empty frames, an exposure of 150 ms was set.

Figure 2 shows an example of a typical image taken during the tests. As described below, the small spots are expected to be due to low energy photons interaction in the gas, while long tracks are expected to be due to high energy electrons produced by natural radioactivity or cosmic rays muons.

The data acquisition is subdivided in *runs*. Each run corresponds to a sample of 400 pictures taken by keeping the detector setup (high voltage values, gas flow, source position) in a stable configuration.

4.4 The ^{55}Fe source

To study the detector response to specific energy deposits in the gas, an ^{55}Fe source was employed. ^{55}Fe decays to ^{55}Mn , producing primarily photons with an energy of 5.9 keV (K_α), with a small fraction of photons at 6.4 keV (K_β). These photons have a mean free path of approximately 22 cm in the GIN gas mixture [24] and interact with the gas molecules through the photoelectric effect, producing electron recoils with similar

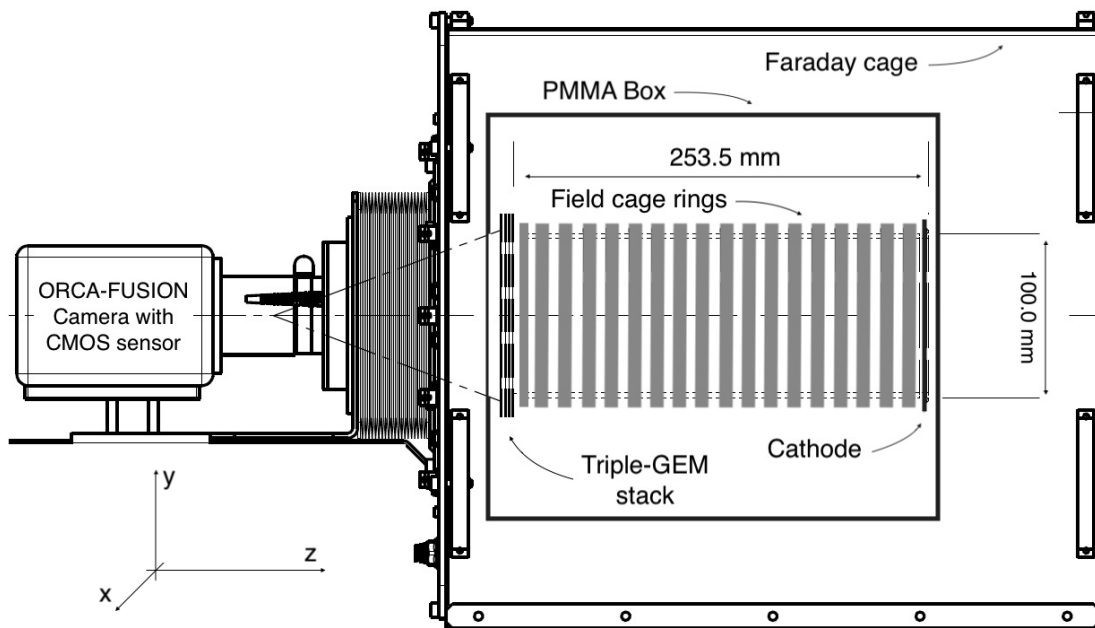


Fig. 1 A lateral sketch of the GIN detector, showing the PMMA vessel and the field cage, the GEM plane and the photo-camera at the left and the cathode on the right. The used reference frame is shown at the bottom.

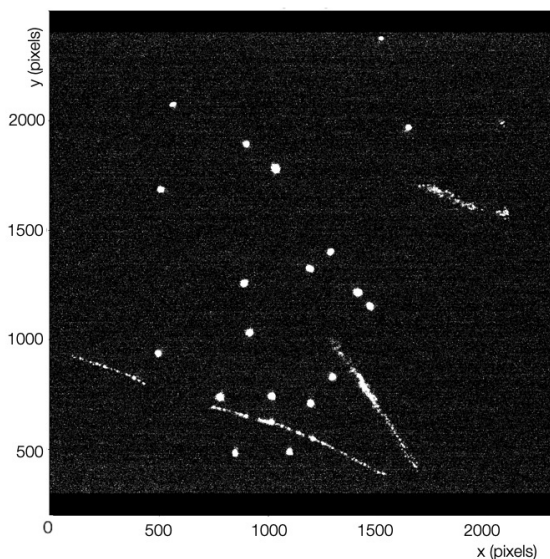


Fig. 2 Example of a typical image collected by the camera during the tests.

energy. These recoils, in turn, ionize gas molecules, creating electron-ion pairs at an average cost of 35 eV per pair. Therefore approximately 168 primary electrons (n_e) are produced in a range of the order of 0.5 mm which represents the expected mean range for electrons of around 6 keV in a He/CF₄ (60/40) mixture at atmospheric pressure.

5 The detector optical response

Under the effect of the drift field, the electrons produced by the absorption of the ⁵⁵Fe photons in the gas, start drifting towards the first GEM, where they are collected within the multiplication channels and initiate the avalanche process.

During their drift, electrons are diffused by the scattering with gas molecules. As a result, the electron cluster will occupy a region that depends on the distance of the interaction point to the GEMs. Their x - y space distribution can be described with a 2-dimensions Gaussian profile having the same standard deviations on x and y ($\sigma_x = \sigma_y = \sigma$). The value of σ depends on the drift distance z through the equation:

$$\sigma = \sqrt{\sigma_0^2 + D_T^2 \cdot z} \quad (2)$$

where σ_0 is the minimum spread due to the diffusion happening in the GEM stack and D_T is the transverse diffusion coefficient, which depends on the gas mixture and the drift field [25].

As already mentioned, on average, for every 100 secondary electrons produced in these multiplication processes, approximately 7 photons are also produced isotropically by the gas. According to the geometrical acceptance (ϵ_Ω), a fraction of the photons produced at the exit of the third GEM, n_p , are collected on the ob-

jective lens, contributing to the image formation on the optical sensor. Thus, given a certain energy release E a proportionality is expected between it, the number of primary electrons $n_e = E/w$ and n_p :

$$n_p = \epsilon_{\Omega} \cdot 0.07 \cdot G_{tot} \cdot n_e \quad (3)$$

where G_{tot} is the total effective electron gain of the triple-GEM stack.

For each ^{55}Fe photon interacting with the gas in the sensitive area of the detector, we expect to observe an image on the sensor containing n_p photons distributed over a circular area, with a density that can be described by a 2D Gaussian profile having a σ dependent on z .

Figure 3 shows on the left two typical examples of light spots as recorded by the optical sensor and produced by the photon interaction in the gas with the ^{55}Fe source at about 4 cm (top) and at about 22 cm (bottom) from the GEM plane. For both cases, the corresponding light profiles along the x and y directions are shown on the right.

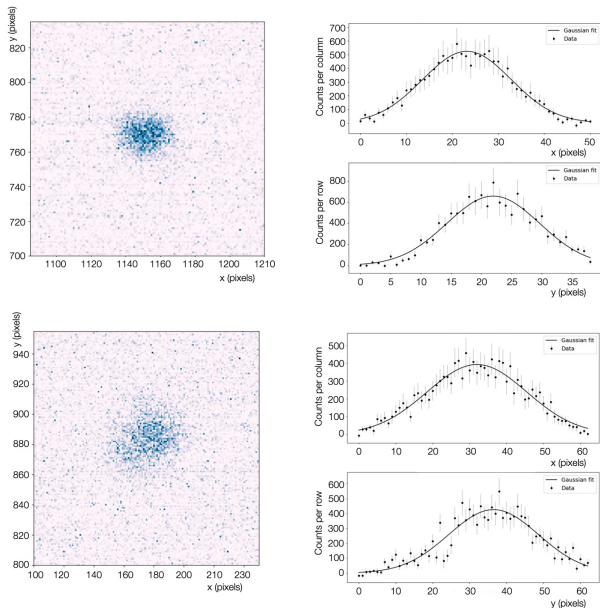


Fig. 3 Left: two examples of a single ^{55}Fe -induced clusters acquired by the camera with source placed at two different distances from the GEM plane. Right: the corresponding light profiles along x and y directions of the clusters, with Gaussian fits superimposed.

The effect of the electron diffusion in the gas is clearly visible: interactions happening farther from the GEMs produce wider spots with a lower maximum number of counts in the central pixels.

6 Cluster reconstruction and analysis

As shown in Fig. 2, in general, images with an exposure time of 150 ms display various signals. Together with the ^{55}Fe -induced clusters with their characteristic round-shape energy deposit, there can be signals generated by interactions in the gas involving gamma rays, X-rays, electrons, or alpha particles due to natural radioactivity, as well as muons from cosmic rays. While muons typically create straight and slim tracks with lengths comparable to the transverse size of the detector, the alphas produce short and very bright tracks. The interactions due to natural radioactivity, given their lower energy, are mostly associated with irregular clusters. In order to select interactions produced by ^{55}Fe , an algorithm developed by the collaboration [26] was employed, capable of identifying groups of pixels hit by photons (clusters) in the images recorded on the sensor, as shown in Fig. 3.

After removing all pixels whose content is deemed compatible with the sensor's electronic noise (zero-suppression), the remaining pixels are processed using this algorithm. The algorithm is based on an upgraded version of DBSCAN [27], which, in addition to considering the spatial density of pixels, weights them on the basis of the amount of collected hits [28]. All pixels identified as belonging to the same spot form a cluster. Figure 4 shows an example of an image containing several light spots with the corresponding reconstructed cluster borders superimposed in red.

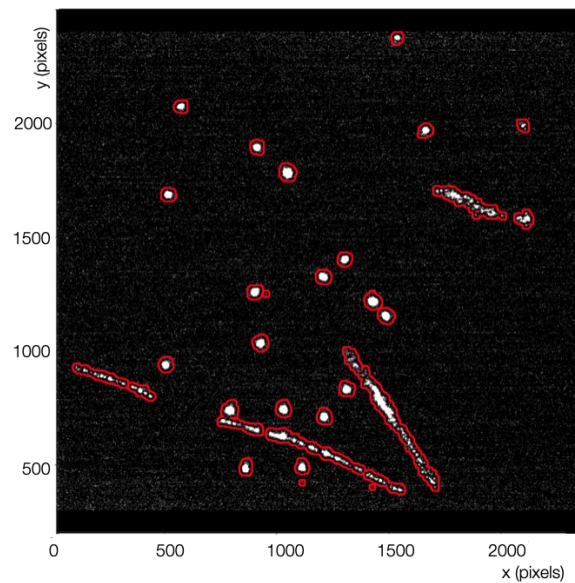


Fig. 4 Example of an image from the camera with superimposed in red the clusters recognised by the reconstruction algorithm.

For all clusters identified as such by the reconstruction algorithm, various characteristics are calculated. Those relevant to the work described in this paper are listed below:

- **Integral** (I_{SC}): the sum of all counts collected by all pixels belonging to the cluster. This variable essentially represents the total light collected in the cluster.
- **Length** and **Width**: these represent the lengths of the major and minor axes, extracted via a Principal Component Analysis (PCA).
- **Slimness** (ξ) evaluated from the ratio (width/length), is related to the cluster shape: the closer it is to one, the more circular the cluster is.
- **Sigma**: the σ of the Gaussian fit performed on the light profile transverse to the major axis.

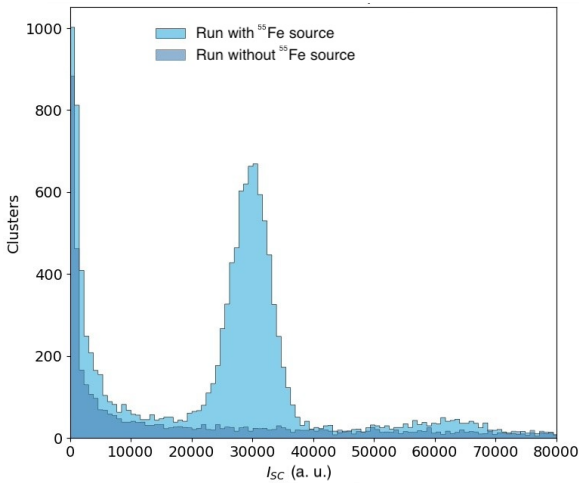


Fig. 5 Distribution of the cluster light integral I_{SC} for data runs with (light blue) and without (royal blue) the ^{55}Fe source.

In Fig. 5 an example of the distributions of the cluster light integral I_{SC} for runs with and without the ^{55}Fe source is shown. The clear peak appearing around 30,000 counts is the one related to absorption of the 5.9 keV. A second bump is visible around 65,000 counts due to two or more rounded ^{55}Fe clusters that are close to each other and are merged by the reconstruction algorithm, resulting in a single cluster.

7 Selection of ^{55}Fe -induced clusters

By using the reconstructed variables for each cluster the selection of spots that can be associated with photon interactions from the ^{55}Fe source is carried out.

Based on studies and optimisation performed in previous studies [12, 29], the following conditions are applied:

- In order to reject fake clusters resulting from electronic noise overfluctuations in the light sensor, a lower threshold of I_{SC} larger than 10,000 units is imposed. Simultaneously, to reduce the selection of merged-clusters, an upper limit of I_{SC} lower than 60,000 is required.
- A maximum length of 7.5 mm is required. Since the spots produced by the source are expected to have dimensions of a few mm^2 , tracks longer than the optimised value are excluded to rejection most cosmic muon tracks while still accepting tracks from ^{55}Fe photon interactions, whose width is larger than the expected range in the gas because of the diffusion effect.
- The parameter ξ is considered, where values closer to 0 correspond to a more elongated cluster, such as the elongated tracks produced by muons, while values near to 1 represent more round clusters. As found in previous studies [23], the ξ value for clusters induced by the source peaks at approximately $\xi = 0.9$, and the range $0.7 < \xi < 1$ contains the majority of ^{55}Fe source clusters.

8 Space position of the interaction points

For the tests described in this article, a special collimator was realised. The collimator features a rectangular slit measuring $0.5 \text{ mm} \times 5 \text{ mm}$. This design allows for relatively uniform illumination of the sensitive volume in the plane parallel to the slit's long side, while simultaneously selecting a well-defined region in the orthogonal direction.

Figures 6 and 7 illustrate, the reconstructed positions on the x - y plane for all events (left panels) and for those selected as due to the ^{55}Fe source (right panels), with the collimator oriented in two configurations:

- **Figure 6** the collimator is positioned with the slit's long side parallel to the GEMs. In this configuration, the interactions are distributed fairly uniformly, spanning 5 cm upwards and 8 cm downwards, covering approximately 65% of the total area.
- **Figure 7** the collimator is rotated such that the slit's long side is orthogonal to the GEMs. Here, the effect of the shorter dimension is evident, with interactions concentrated within a region measuring 1.7 cm upwards and 3.4 cm downwards.

In both configurations, the selection process effectively rejects the majority of events that are not expected to originate from the ^{55}Fe source which are ex-

pected to be uniformly distributed in the x - y plane, as observed in runs without the source.

The RMS of the z -position distribution of the interaction points was found to be about 0.5 cm when the collimator slit was aligned parallel to the GEM plane.

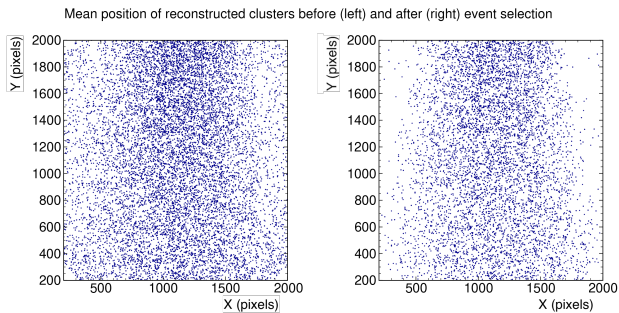


Fig. 6 Maps of the positions of all the reconstructed clusters (left) and of the ones expected to be due to the interaction of the ^{55}Fe photons (right) with the collimator slit parallel to the GEM plane.

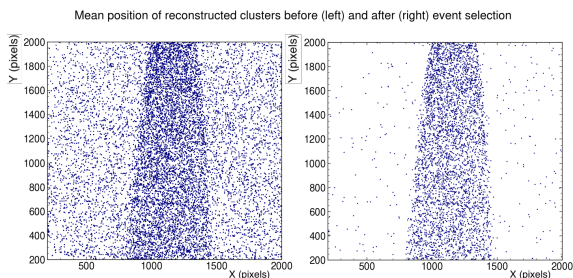


Fig. 7 Maps of the positions of all the reconstructed clusters (left) and of the ones expected to be due to the interaction of the ^{55}Fe photons (right) with the collimator slit orthogonal to the GEM plane.

9 The detector response as a function of the ^{55}Fe source position

Using the ^{55}Fe source, the detector response as a function of the ionization point distance from the GEM plane has been studied. For this study, data-runs were collected both in the absence of the ^{55}Fe source and in its presence, placing the source at ten different distances from the GEM plane ($z_{^{55}\text{Fe}}$), spaced 2 cm apart, ranging from about 4 cm to about 22 cm.

9.1 Spot size and electron diffusion

As discussed in Sect. 5 and shown in Eq. 2, primary electron diffuse during their drift along z towards the

GEMs. They are therefore expected to spread over a region on the GEM plane that increases with the drift distance.

For each run, after applying the event selection described in Sect. 7, for all clusters attributed to ^{55}Fe , the quantities introduced in Sect. 6 are then evaluated.

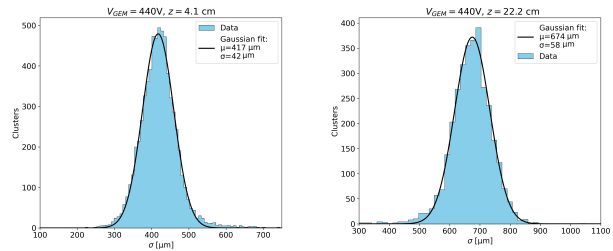


Fig. 8 Distributions of the σ values evaluated for the clusters attributed to the ^{55}Fe interactions for the source positions $z_{^{55}\text{Fe}} = 2.1$ cm (left) and $z_{^{55}\text{Fe}} = 22.2$ cm (right) with a superimposed Gaussian fit.

In Fig. 8 two examples of distributions of σ values are shown for interactions occurred nearer (left) or farther (right) to the GEM plane. It can be clearly seen that due to the effect of the diffusion the mean value increases for large distances.

The mean values of the σ distributions, squared, are shown in the plots in Fig. 9 as a function of the distance z of the source from the GEMs.

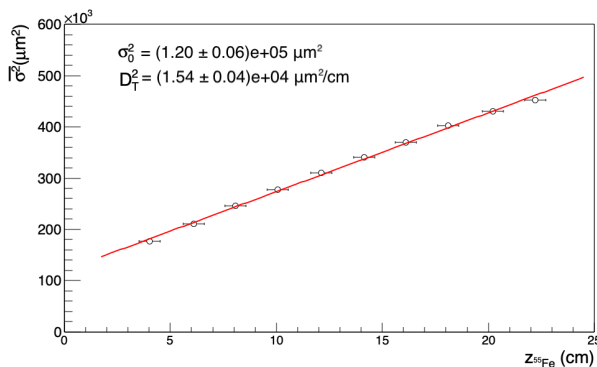


Fig. 9 Average values of the σ distribution, squared, as a function of the position $z_{^{55}\text{Fe}}$, with a superimposed linear fit. Vertical uncertainties on the points are the statistical uncertainties from the Gaussian fits, while horizontal ones describe the spread in z of the interactions as described in Sec. 8.

A linear fit is superimposed, yielding the following estimates for σ_0 and the transverse diffusion coefficient (D_T) at 1.0 kV/cm:

$$\sigma_0 = (346 \pm 10) \mu\text{m} \quad (4)$$

$$D_T = (124 \pm 2) \frac{\mu\text{m}}{\sqrt{\text{cm}}} \quad (5)$$

These values are in good agreement with what was evaluated with Garfield and measured with a different setup by our collaboration [30,31,32].

9.2 Spot light

The distributions of I_{SC} values, representing the total light in the spot, were also studied for different values of $z^{55\text{Fe}}$ and V_{GEM} . In particular for $V_{\text{GEM}} = 440$ V, data were taken for the same source positions described in the previous section, while other data at a voltage of $V_{\text{GEM}} = 430$ V and $V_{\text{GEM}} = 420$ V, were only taken for $z^{55\text{Fe}} = 4$ cm, 8 cm, 12 cm, 16 cm, and 20 cm. For each run, the distribution of I_{SC} for all the clusters satisfying the ^{55}Fe selection is filled, and is shown in Fig. 10 for different V_{GEM} and $z^{55\text{Fe}}$.

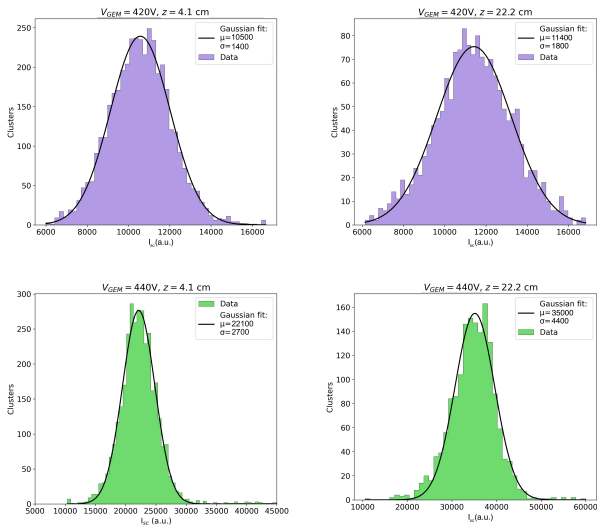


Fig. 10 Distributions of the values of the light integral (I_{SC}) evaluated for the all clusters attributed to the ^{55}Fe interactions for $V_{\text{GEM}} = 420$ V (top) and $V_{\text{GEM}} = 440$ V (bottom) with the source in two different positions with a gaussian fit superimposed.

As described in Sec. 5 and in Eq. 3, a direct proportionality between the light in the spot and the number of primary ionised electrons is expected. Therefore, while different values of V_{GEM} are expected to have large impact on the total amount of charge and light produced, since the gain should be independent from the event depth in the gas volume, the mean values of the aforementioned distributions should ideally remain independent from $z^{55\text{Fe}}$.

From Fig. 10 it is possible to see how, instead, the amount of collected light increases as $z^{55\text{Fe}}$ increases for all values of V_{GEM} .

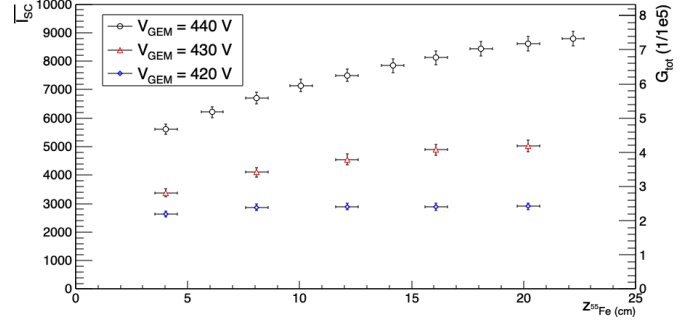


Fig. 11 Average I_{SC} and gas gain values measured at different distances from the GEM plane for V_{GEM} values of 440 V (black), 430 V (red), and 420 V (blue). The horizontal bars indicate the spread in z of the photon interaction points as described in Sec. 8; the vertical bars take into account not only the statistical fluctuations of the mean values of the gaussian fits, but also other uncertainties (due for example to environmental conditions) and evaluated by comparing independent measures repeated in the same configurations.

The behaviour of I_{SC} and the corresponding G_{tot} values evaluated by means of Eq. 3, for different $z^{55\text{Fe}}$ and three different V_{GEM} values (all $V_{\text{GEM}} = 440$ V, 430 V and 420 V) are shown in Fig. 11 as a function of the source position. Vertical bars account for the statistical fluctuations of the mean values of the gaussian fits and for other uncertainties (due for example to environmental conditions) that were evaluated by comparing independent measures repeated in the same configurations.

On the one hand, it is clearly observed that the total light and the gain, for each value of $z^{55\text{Fe}}$, depend on V_{GEM} and increase with it. On the other hand, it is also noticeable that the detector response is not constant and tends to increase for high values of $z^{55\text{Fe}}$ in all cases. This effect was already observed and described in other papers by the CYGNO collaboration [24]. A similar effect had already been observed by other research groups [33]. As described in the next section, our interpretation is that the observed behaviour can be explained as a *gain saturation* occurring for GEMs operating in very high gain conditions and producing a high charge density in the multiplication channels. The electron diffusion, by reducing the charge spatial density, can help in mitigating this effect leading to an increase in the actual gain for ionizations occurring farther from the GEM plane.

10 Gain saturation model

A simple model was developed by the CYGNO collaboration to microscopically explain the phenomena leading to this gain saturation. Let us assume that, during the development of the avalanche within the GEM multiplication channels, a significant amount of electrons and positive ions are produced. Under the effect of the electric field present in the channel, these last slowly migrate towards the lower potential plane of the GEM. Their positive electric charge will tend to partially shield the electric field present in the channel. This effect will decrease the electric field during the development of the avalanche itself, reducing the overall gain. In essence, the actual gain of each channel will depend not only on its operation voltage V_{GEM} , but also on how much charge is produced. The effective screen parameter of the field, denoted as β , is introduced, so that at any given time the electric field effectively accelerating the charges in the channel is given by $E_0(1-\beta n)$ where n is the number of electrons in the channel and E_0 is the electric field produced within the channel by the voltage difference applied to the two GEM sides V_{GEM} . At first order, we can assume a uniform electric field $E_0 = V_{\text{GEM}}/d$ where d is the single GEM thickness. The increase of the number of charges n in a spatial step ds can therefore be described by a modified Townsend [34] equation of the type:

$$\frac{dn}{ds} = \alpha E_0(1 - \beta n)n \quad (6)$$

By integrating this equation, inside the GEM channel:

$$\int_{n_0}^{n_{\text{tot}}} \frac{dn}{(1 - \beta n)n} = \int_0^d \alpha E_0 ds \quad (7)$$

the formula to evaluate the gain of a GEM channel $G = n_{\text{tot}}/n_0$ with a voltage drop V_{GEM} can be obtained:

$$G = \frac{ce^{\alpha V_{\text{GEM}}}}{1 + \beta n_0(ce^{\alpha V_{\text{GEM}}} - 1)}. \quad (8)$$

The *no-saturated gain* showing the usual exponential behaviour foreseen by the Townsend formula can be indicated as $\tilde{G} = ce^{\alpha V_{\text{GEM}}}$ where c is a normalization factor typically used to account for the deviation from ideal exponential gain behavior, especially at low voltages [35]. Eq. 8 can be rewritten as:

$$G = \frac{\tilde{G}}{1 + \beta n_0(\tilde{G} - 1)} \quad (9)$$

It should be noticed that it depends on the product of the parameter β and the number of primary electrons

entering the channel n_0 and on V_{GEM} . In particular, it can be observed that:

- **a)** if $\beta n_0 \simeq 0$ (i.e. negligible screen effect), G is equal to \tilde{G} (the no-saturated gain);
- **b)** if $\beta n_0 \simeq 1$ then $G \simeq 1$, the saturation fully suppresses the gain in the GEM channel, giving, ideally, $n_{\text{tot}} = n_0$.

These considerations allow to interpret β as the inverse of the equivalent number of *effective charges* n_{eq} present on the two sides of the channel to generate its internal field: $\beta \simeq 1/n_{eq}$. If the number n_0 of charges entering the channel is already close to n_{eq} , the resulting electric field is zero and in the GEM there will be no multiplication. Therefore, the dependence of β on V_{GEM} can be made explicit as $\beta = r/V_{\text{GEM}}$ with a parameter r that depends on the GEM foil capacitance.

Let us now assume that in the first two GEMs (GEM₁ and GEM₂), the total amount of charge is low enough to be in the case (a) above and that the gain saturation only effects GEM₃ (i.e. $\tilde{G}_1 = G_1$ and $\tilde{G}_2 = G_2$).

Electrons ionised in the gas volume at a certain z , after the drift and the multiplication processes in the first two GEMs, produce an electron cloud with a space distribution that can be modeled as a 3D normal distribution with variance σ . The volume of the electron cloud will then be proportional to σ^3 .

Thus, in GEM₃, the amount of charge collected by each channel n_0 :

- depends on the primary ionisation in the gas n_e ;
- is proportional to k/σ^3 where k takes into account the GEM channels dimensions and density;
- increases as the product of the gains of G_1 and G_2 ;

Let's now suppose that the GEMs operate at the same V_{GEM} . Therefore, $\tilde{G}_1 = \tilde{G}_2 = \tilde{G}_3 = \tilde{G} = ce^{\alpha V_{\text{GEM}}}$. The total gain of the triple-GEM stack can be written as:

$$G_{\text{tot}} = G_1 \cdot G_2 \cdot G_3 = \frac{(ce^{\alpha V_{\text{GEM}}})^3 \sigma^3}{\sigma^3 + (p/V_{\text{GEM}})(ce^{\alpha V_{\text{GEM}}})^2(ce^{\alpha V_{\text{GEM}}} - 1)} \quad (10)$$

where the parameter p accounts for r and k .

Figure 12 illustrates the behaviour of G_{tot} as a function of $\bar{\sigma}$, as measured in the data for $V_{\text{GEM}} = 440$ V, $V_{\text{GEM}} = 430$ V, and $V_{\text{GEM}} = 420$ V. These measurements are also the same entering in Figs. 9 and 11.

The curves overlaid on the data points represent the results of a simultaneous fit to the three parameters entering Eq. 10, fully correlated among the three sets of data at different V_{GEM} .

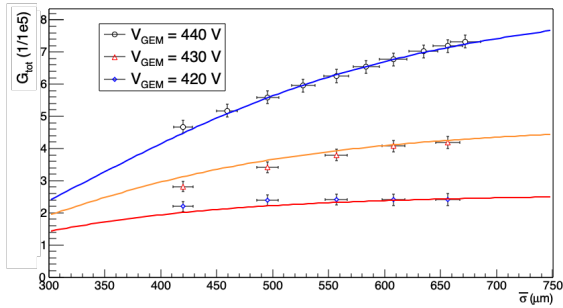


Fig. 12 Charge gain as a function of the average spot σ , values for the Triple-GEM stack in three configurations: all $V_{\text{GEM}} = 440$ V, all $V_{\text{GEM}} = 430$ V and all $V_{\text{GEM}} = 420$ V with superimposed the curves representing the results of a simultaneous fit to the three parameters entering Eq. 10.

The parameter values extracted from the fit are as follows:

$$\begin{aligned}\alpha &= (2.06 \pm 0.02) \times 10^{-2} \text{V}^{-1}, \\ c &= (1.13 \pm 0.06) \times 10^{-2}, \\ p &= (3.7 \pm 0.2) \times 10^4 \mu\text{m}^3 \text{V}.\end{aligned}$$

These parameters also allow for the evaluation of the no-saturated gains (\tilde{G}) for the tested V_{GEM} values:

$$\begin{aligned}\tilde{G}(V_{\text{GEM}} = 440\text{V}) &= 97 \pm 9 \\ \tilde{G}(V_{\text{GEM}} = 430\text{V}) &= 79 \pm 7 \\ \tilde{G}(V_{\text{GEM}} = 420\text{V}) &= 64 \pm 5\end{aligned}$$

To assess the reliability of the curves resulting from the fit, the distribution of their normalized residuals to the data was studied. An RMS value of 0.04 was obtained indicating that, across the entire range of gain values, spanning approximately from 2×10^5 to 7×10^5 , the proposed model describes the gain dependence on the charge density within 4%.

Considering the approximations made (namely, that the electric field in the channel is uniform and that the charge distribution within the cloud is uniform, resulting in a constant density), this results proves the proposed model with a percent accuracy.

This analytical model can therefore also be used for numerical simulations of the gain behaviour of GEMs, to predict their behaviour under conditions of gain and release of energies other than those of this work.

11 Conclusion

In this study, the light response of an optically readout GEM-based TPC developed for the CYGNO experiment was investigated. Through a systematic analysis

of experimental data collected with a two-liter prototype, the dependence of the response of detector on the charge density and spatial distribution of ionization electrons was studied and characterised. The obtained results confirm the existence of a gain reduction effect attributed to space-charge buildup within the multiplication channels of the GEM.

From the study of the shape and the total amount of photons of the light spots induced by ^{55}Fe X-rays, key parameters such as transverse diffusion and light yield variations as a function of the drift distance were extracted. A phenomenological model describing gain saturation effects due to space-charge accumulation was developed, which successfully reproduces the observed trends in experimental data with a precision of a few percent.

These findings not only confirm the presence of a space charge effect that impacts the response linearity, but also validate a mathematical model capable of predicting this behaviour, which can be used to simulate the response of GEM detectors in presence of high primary charge density.

In particular, these results will contribute to the development and optimisation of the design of optically readout TPC ensuring reliable operation under high-gain conditions.

Acknowledgements This project has received fundings under the European Union's Horizon 2020 research and innovation program from the European Research Council (ERC) grant agreement No 818744 and is supported by the Italian Ministry of Education, University and Research through the project PRIN: Progetti di Ricerca di Rilevante Interesse Nazionale "Zero Radioactivity in Future experiment" (Prot. 2017T54J9J). We want to thank General Services and Mechanical Workshops of Laboratori Nazionali di Frascati (LNF).

References

1. F.D. Amaro, E. Baracchini, L. Benussi, S. Bianco, C. Capocchia, M. Caponero, D.S. Cardoso, G. Cavoto, A. Cortez, I.A. Costa, R.J.d.C. Roque, E. Dané, G. Dho, F. Di Giambattista, E. Di Marco, G. Grilli di Cortona, G. D'Imperio, F. Iacoangeli, H.P. Lima Júnior, G.S. Pinheiro Lopes, A.d.S. Lopes Júnior, G. Maccarrone, R.D.P. Mano, M. Marafini, R.R. Marcelo Gregorio, D.J.G. Marques, G. Mazzitelli, A.G. McLean, A. Messina, C.M. Bernardes Monteiro, R.A. Nobrega, I.F. Pains, E. Paoletti, L. Passamonti, S. Pelosi, F. Petrucci, S. Piacentini, D. Piccolo, D. Pierluigi, D. Pinci, A. Prajapati, F. Renga, F. Rosatelli, A. Russo, J.M.F. dos Santos, G. Saviano, N.J.C. Spooner, R. Tesaro, S. Tomassini, S. Torelli, *Instruments* **6**(1) (2022). doi:10.3390/instruments6010006. URL <https://www.mdpi.com/2410-390X/6/1/6>
2. G. Bertone, D. Hooper, *Rev. Mod. Phys.* **90**, 045002 (2018). doi:10.1103/RevModPhys.90.045002.

- URL <https://link.aps.org/doi/10.1103/RevModPhys.747.90.045002> ⁷⁴⁷
3. S.E. Vahsen, C.A.J. O'Hare, W.A. Lynch, N.J.C. Spooner, E. Baracchini, P. Barbeau, J.B.R. Battat, B. Crow, C. Deaconu, C. Eldridge, A.C. Ezeribe, M. Ghrear, D. Loomba, K.J. Mack, K. Miuchi, F.M. Mou-ton, N.S. Phan, K. Scholberg, T.N. Thorpe. Cygnus: Feasibility of a nuclear recoil observatory with directional sensitivity to dark matter and neutrinos (2020). URL <https://arxiv.org/abs/2008.12587> ⁷⁵⁵
 4. S.E. Vahsen, et al., (2020) ⁷⁵⁷
 5. C. Deaconu, M. Leyton, R. Corliss, G. Druitt, R. Eggleston, N. Guerrero, S. Henderson, J. Lopez, J. Monroe, P. Fisher, Phys. Rev. D **95**, 122002 (2017). doi:10.1103/PhysRevD.95.122002. URL <https://link.aps.org/doi/10.1103/PhysRevD.95.122002> ⁷⁶¹
 6. F. Sauli, Nucl. Instrum. Meth. A **386**, 531 (1997). doi:10.1016/S0168-9002(96)01172-2 ⁷⁶⁴
 7. M. Fraga, F. Fraga, S. Fetal, L. Margato, R. Marques, A. Policarpo, Nuclear Instruments and Methods in Physics Research Section A: Accelerators, Spectrometers, Detectors and Associated Equipment **504**(1), 88 (2003). doi:[https://doi.org/10.1016/S0168-9002\(03\)00758-7](https://doi.org/10.1016/S0168-9002(03)00758-7). URL <http://www.sciencedirect.com/science/article/pii/S0168900203007587>. Proceedings of the 3rd International Conference on New Developments in Photodetection ⁷⁷³
 8. M.M.F.R. Fraga, F.A.F. Fraga, S.T.G. Fetal, L.M.S. Margato, R. Ferreira-Marques, A.J.P.L. Policarpo, Nucl. Instrum. Meth. **A504**, 88 (2003). doi:10.1016/S0168-9002(03)00758-7 ⁷⁷⁷
 9. M. Cwiok, W. Dominik, Z. Janas, A. Korgul, K. Miernik, M. Pfutzner, M. Sawicka, A. Wasilewski, IEEE Transactions on Nuclear Science **52**(6), 2895 (2005) ⁷⁷⁹
 10. V.C. Antochi, E. Baracchini, G. Cavoto, E.D. Marco, M. Marafini, G. Mazzitelli, D. Pinci, F. Renga, S. Tomassini, C. Voena, JINST **13**(05), P05001 (2018). doi:10.1088/1748-0221/13/05/P05001 ⁷⁸³
 11. A. Morozov, L.M.S. Margato, M.M.F.R. Fraga, L. Pereira, F.A.F. Fraga, JINST **7**, P02008 (2012). doi:10.1088/1748-0221/7/02/P02008 ⁷⁸⁶
 12. I.A. Costa, E. Baracchini, F. Bellini, L. Benussi, S. Bianco, M. Caponero, G. Cavoto, G. D'Imperio, E.D. Marco, G. Maccarrone, M. Marafini, G. Mazzitelli, A. Messina, F. Petrucci, D. Piccolo, D. Pinci, F. Renga, F. Rosatelli, G. Saviano, S. Tomassini, Journal of Instrumentation **14**(07), P07011 (2019). doi:10.1088/1748-0221/14/07/p07011 ⁷⁹²
 13. G.F. Reinking, L.G. Christophorou, S.R. Hunter, Journal of Applied Physics **60**, 499 (1986). doi:10.1063/1.337792. URL <https://doi.org/10.1063/1.337792> ⁷⁹⁶
 14. I.C. Wolfe, Measurement of work function in cf4 gas. Master's thesis, Massachusetts Institute of Technology (2010). Master's thesis ⁷⁹⁹
 15. P.A. Zyla, et al. (Particle Data Group), Progress of Theoretical and Experimental Physics **2020**(8), 083C01 (2020). doi:10.1093/ptep/ptaa104. URL <https://doi.org/10.1093/ptep/ptaa104> ⁸⁰²
 16. S. Vahsen, K. Oliver-Mallory, M. Lopez-Thibodeaux, J. Kadyk, M. Garcia-Sciveres, Nuclear Instruments and Methods in Physics Research Section A **738**, 111 (2014). doi:10.1016/j.nima.2013.12.034 ⁸⁰⁷
 17. M. Marafini, V. Patera, D. Pinci, A. Sarti, A. Sciubba, N.M. Torchia, IEEE Transactions on Nuclear Science **65**, 604 (2018). doi:10.1109/TNS.2017.2778503 ⁸¹⁰
 18. M. Marafini, V. Patera, D. Pinci, A. Sarti, A. Sciubba, E. Spiriti, Nucl. Instrum. Meth. **A845**, 285 (2017). doi:10.1016/j.nima.2016.04.014 ⁸¹³
 19. M. Marafini, V. Patera, D. Pinci, A. Sarti, A. Sciubba, E. Spiriti, JINST **10**(12), P12010 (2015). doi:10.1088/1748-0221/10/12/P12010
 20. M. Marafini, V. Patera, D. Pinci, A. Sarti, A. Sciubba, E. Spiriti, Nuclear Instruments and Methods in Physics Research Section A: Accelerators, Spectrometers, Detectors and Associated Equipment **824**, 562 (2016). doi:<https://doi.org/10.1016/j.nima.2015.11.058>. URL <http://www.sciencedirect.com/science/article/pii/S0168900215014230>. Frontier Detectors for Frontier Physics: Proceedings of the 13th Pisa Meeting on Advanced Detectors
 21. E. Baracchini, et al., JINST **15**(08), P08018 (2020). doi:10.1088/1748-0221/15/08/P08018
 22. F.D. Amaro, et al., Eur. Phys. J. C **84**(10), 1122 (2024). doi:10.1140/epjc/s10052-024-13471-5
 23. E. Baracchini, et al., Measur. Sci. Tech. **32**(2), 025902 (2021). doi:10.1088/1361-6501/abbd12
 24. F.D. Amaro, R. Antonietti, E. Baracchini, L. Benussi, S. Bianco, F. Borra, C. Capoccia, M. Caponero, D.S. Cardoso, G. Cavoto, I.A. Costa, E. Dané, G. Dho, F. Di Giambattista, E. Di Marco, G. D'Imperio, J.M.F. dos Santos, G.G. di Cortona, F. Iacoangeli, E. Kemp, H.P.L. Júnior, G.S.P. Lopes, A.d.S.L. Júnior, G. Maccarrone, R.D.P. Mano, R.R.M. Gregorio, D.J.G. Marques, G. Mazzitelli, A.G. McLean, P. Meloni, A. Messina, C.M.B. Monteiro, R.A. Nobrega, I.F. Pains, E. Paoletti, L. Passamonti, S. Pelosi, F. Petrucci, S. Piacentini, D. Piccolo, D. Pierluigi, D. Pinci, A. Prajapati, F. Renga, R.C. Roque, F. Rosatelli, A. Russo, G. Saviano, N.J.C. Spooner, R. Tesauero, S. Tomassini, S. Torelli, D. Tozzi, European Physical Journal C **83**(10), 946 (2023). doi:10.1140/epjc/s10052-023-11988-9
 25. F. Sauli, Principles of operation of multiwire proportional and drift chambers. Tech. rep., Geneva (1977). doi:10.5170/CERN-1977-009. URL <https://cds.cern.ch/record/117989>. CERN, Geneva, 1975 - 1976
 26. E. Baracchini, et al., JINST **15**(12), T12003 (2020). doi:10.1088/1748-0221/15/12/T12003
 27. M. Ester, H.P. Kriegel, J. Sander, X. Xu, in *Knowledge Discovery and Data Mining* (1996). URL <https://api.semanticscholar.org/CorpusID:355163>
 28. F.D. Amaro, R. Antonietti, E. Baracchini, L. Benussi, S. Bianco, F. Borra, C. Capoccia, M. Caponero, D.S. Cardoso, G. Cavoto, I.A. Costa, G. D'Imperio, E. Dané, G. Dho, F.D. Giambattista, E.D. Marco, F. Iacoangeli, E. Kemp, H.P.L. Júnior, G.S.P. Lopes, G. Maccarrone, R.D.P. Mano, R.R.M. Gregorio, D.J.G. Marques, G. Mazzitelli, A.G. McLean, P. Meloni, A. Messina, C.M.B. Monteiro, R.A. Nobrega, I.F. Pains, E. Paoletti, L. Passamonti, F. Petrucci, S. Piacentini, D. Piccolo, D. Pierluigi, D. Pinci, A. Prajapati, F. Renga, R.J. d C Roque, F. Rosatelli, A. Russo, G. Saviano, N.J.C. Spooner, R. Tesauero, S. Tomassini, S. Torelli, D. Tozzi, J.M.F. dos Santos, Measurement Science and Technology **34**(12), 125024 (2023). doi:10.1088/1361-6501/acf402. URL <https://dx.doi.org/10.1088/1361-6501/acf402>
 29. I.A. Costa, E. Baracchini, F. Bellini, L. Benussi, S. Bianco, M. Caponero, G. Cavoto, G. D'Imperio, E.D. Marco, G. Maccarrone, M. Marafini, G. Mazzitelli, A. Messina, F. Petrucci, D. Piccolo, D. Pinci, F. Renga, F. Rosatelli, G. Saviano, S. Tomassini, Journal of Instrumentation **14**(07), P07011 (2019). doi:10.1088/1748-0221/14/07/p07011. URL <https://doi.org/10.1088/1748-0221/14/07/p07011>
 30. E. Baracchini, L. Benussi, S. Bianco, C. Capoccia, M. Caponero, G. Cavoto, A. Cortez, I.A. Costa,

- 814 E.D. Marco, G. D’Imperio, G. Dho, F. Iacoangeli,
815 G. Maccarrone, M. Marafini, G. Mazzitelli, A. Messina,
816 R.A. Nobrega, A. Orlandi, E. Paoletti, L. Passamonti,
817 F. Petrucci, D. Piccolo, D. Pierluigi, D. Pinci, F. Renga,
818 F. Rosatelli, A. Russo, G. Saviano, S. Tomassini, *Journal of Instrumentation* **15**(10), P10001–P10001 (2020).
819 doi:10.1088/1748-0221/15/10/p10001. URL <http://dx.doi.org/10.1088/1748-0221/15/10/p10001>.
820 doi:10.1088/1748-0221/15/10/P10001
821
- 822 31. R. Campagnola, Study and optimization of the light-
823 yield of a triple-GEM detector . Master’s thesis, Sapienza
824 University of Rome (2018). URL <https://cds.cern.ch/record/2313231/files/CERN-THESIS-2018-027.pdf>
825
- 826 32. E. Baracchini, et al., *JINST* **15**(10), P10001 (2020).
827 doi:10.1088/1748-0221/15/10/P10001
- 828 33. S. Franchino, D.G. Diaz, R. Hall-Wilton, H. Muller,
829 E. Oliveri, D. Pfeiffer, F. Resnati, L. Ropelewski,
830 M.V. Stenis, C. Streli, P. Thuiner, R. Veenhof, in
831 *2015 IEEE Nuclear Science Symposium and Medical Imaging Conference (NSS/MIC)* (IEEE, 2015).
832 doi:10.1109/nssmic.2015.7581778. URL <https://doi.org/10.1109/nssmic.2015.7581778>.
833 doi:10.1109/nssmic.2015.7581778
834
- 835 34. W.R. Leo, *Techniques for Nuclear and Particle Physics Experiments* (Springer, 1994). doi:10.1007/978-3-642-57920-2
836
- 837
- 838 35. D. Pinci, A triple-GEM detector for the muon system of
839 the LHCb experiment. Ph.D. thesis, Cagliari University,
840 CERN-THESIS-2006-070 (2006). URL <http://weblib.cern.ch/abstract?CERN-THESIS-2006-070>
841